Untying the Gordian KNOT: Unbiased Single Particle Tracking Using Point Clouds and Adaptive Motion Analysis

Jorge Zepeda O†, Logan D. C. Bishop‡, Chayan Dutta‡, Suparna Sarkar-Banerjee‡, Wesley W. Leung§, Christy F. Landes†‡‖*

† Department of Electrical and Computer Engineering, Rice University, Houston, Texas 77005, United States

‡ Department of Chemistry, Rice University, Houston, Texas 77005, United States

§ Applied Physics Graduate Program, Smalley-Curl Institute, Rice University, Houston, Texas 77005, United States

‖ Department of Chemical and Biomolecular Engineering, Rice University, Houston, Texas 77005, United States

Corresponding Author

*Christy F. Landes

Department of Chemistry, Rice University, Houston, Texas, Tel: (713) 348-4232,

Email: cflandes@rice.edu.

Keywords: single particle tracking, deconvolution, point clouds, single frame displacement, particle motion classification

Abstract:

Achieving mechanistic understanding of transport in complex environments such as inside cells or at polymer interfaces is challenging. We need better ways to image transport in 3-D and better single particle tracking algorithms to determine that transport that are not systemically biased towards any classical motion model. Here we present an unbiased single particle tracking algorithm, Knowing Nothing Outside Tracking (KNOT). KNOT uses point clouds provided by iterative deconvolution to educate individual particle localizations and link particle positions between frames to achieve 2-D and 3-D tracking. Information from prior point clouds fuels an independent adaptive motion model for each particle to avoid global models that could introduce biases. KNOT competes with or surpasses other 2-D methods from the 2012 particle tracking challenge while accurately tracking adsorption dynamics of proteins on polymer surfaces and early endosome transport in live cells in 3-D. We apply KNOT to study 3-D endosome transport to reveal new physical insight about locally directed and diffusive transport in live cellular environment. Our analysis demonstrates better accuracy in classifying local motion and its direction compared to previous methods, revealing intricate intracellular transport heterogeneities.

Introduction:

Single particle tracking is used to understand the complex mechanistic transport involved during intracellular processes such as endocytosis,[1] protein or DNA trafficking,[2-4] endosomal trafficking,[5] and drug delivery[6] and to understand protein-polymer interactions during protein separations.[7-11] However, three problems hinder particle motion analysis: capturing simultaneous particle positions in 3-D, resolving ambiguous positions such as during particle overlap or photoblinking, and tracking the stochastic changes between diffusive and directed motion without bias. The first problem is routinely addressed through methods such as light sheet microscopy,[12, 13] intensity decay during total internal reflection microscopy,[14] multiplane imaging using prisms,[15] multiple beam splitters,[16] or piezo stages,[17] and point spread function (PSF) engineering. PSF engineering requires little additional experimental equipment (a 4*f* system and either a phase mask[18] or a spatial light modulator[19-22]) to expose the 3-D position of particles, using digital signal processing to deconvolve a 2-D widefield image taken with a known phase mask PSF.[18-24] Resolving ambiguous particle positions relies on extrapolating a known motion model to the frame in question.[25-27] Also, true dynamics can be obscured due to mixed motion[28] as no individual model captures the nuances of confined, diffusive, and directed motion simultaneously.[29-31] Correctly classifying particle motion in a heterogenous environment is necessary for detecting endosomal movements during cellular changes in cancer.[32]

Tracking using predetermined global motion models is fast, but can bias observed motion,[33] leading to misclassification of intracellular particle dynamics.[30] The nearest neighbors method links the nearest available candidate for each particle, which excels in tracking uniformly random motion such as diffusion,[34-36] but fails to accurately describe the trajectory overlaps commonly observed in directed motion along microtubule pathways.[25, 37] Autoregressive methods

link candidates with similar displacements to the most recent link, which accurately depicts directed motion,[38, 39] but can fail to follow stochastic motion.[26, 38] The specialization of nearest neighbors and autoregression require the user to estimate the most common motion present in a sample before tracking, especially for high particle density measurements, a choice with vastly different results if particle motion is evenly distributed between directed and diffusive. Other tracking approaches optimize local or global statistics, such as total displacement, or follow multiple hypotheses to accommodate for diverse particle behaviors. However, these static methods can still bias results towards one or more inherent optimization functions[26, 40, 41] or statistical structures[39, 42] when faced with mixed motion.

Adaptive tracking analyzes a local window of behavior to propagate self-consistencies in prior motion to track dynamic particle behavior rather than restrict trajectories to pre-established models, avoiding supervisory biases.[43] Algorithms that use multiple hypothesis testing either switch between multiple motion models[31, 33, 44] or evaluate many possible trajectories[26, 40, 41] to track mixed motion mitigate the bias of each model used at the cost of increased computational complexity. Adaptive tracking algorithms avoid exhaustive model or trajectory searching by promoting candidate displacements consistent with a window of recent observations, thereby decreasing the overall computational complexity while maintaining accuracy and adaptability.[45] Point clouds are the suitable unit of measure for particle position in an adaptive tracking method because point clouds contain multiple weighted data points,[46, 47] adapting to a localization confidence gradient rather than a single representative point. Achieving accurate particle linking in a cellular environment with an adaptive tracker could lead to fundamental discoveries about endosomal transport mechanisms. For example, being able to accurately determine the directed or diffusive motion of endosomes could lead to a directional analysis of what endosomes move

towards the Golgi apparatus or other areas of interest for a given cargo when mapping the endosomal transport mechanisms within the cell.[3]

We present an adaptive tracking method, Knowing Nothing Outside Tracking (KNOT), that combines phase engineering and point cloud displacement analysis to detect and track particles adaptively in both 2-D and 3-D. We quantify the 2-D performance of KNOT with the 2012 particle tracking challenge data[48] and the 3-D capabilities by tracking lysozyme adsorption to poly N-isopropylacrylamide-co-allylamine (pNIPAM-co-AA) hydrogels and $Rab5^+$ early endosome transport in live cells. Without knowledge of particle motion, KNOT outperforms nearest neighbors or autoregressive trackers and competes with more complex trackers. Additionally, we show that KNOT distinguishes directed from non-directed motion more accurately than traditional mean squared displacement (MSD) or temporal MSD (tMSD) analysis. Local motion analysis demonstrates that endosomes are predominantly directed towards the zenith or laterally with respect to the plane of measurement. KNOT accounts for diffusive, directed, and mixed motion using the same approach, thus becoming a universal single particle tracking method.

Experimental section:

Materials and methods:

Software: Software details are presented in the Supporting Information online.

Polystyrene bead preparation: Carboxylate-modified polystyrene (PS) 100 nm beads (orange fluorescent, Invitrogen) were diluted by a factor of 1:1000 from stock concentration in HEPES buffer (Sigma, 10 mM, PH = 7.3). Microscope coverslips (22 × 22 mm, no. 1; VWR) were sequentially sonicated for 5 min in DI water, ethanol, and acetone. Coverslips were then immersed in base piranha solution containing 4% (v/v) H_2O_2 (Fisher Scientific) and 13% (v/v) NH_4OH

(Sigma, ACS grade) for 30 min at 80 °C. After thorough rinsing with DI water, the coverslips were treated with oxygen plasma for 2 min (PDC-32G; Harrick Plasma, Ithaca, NY). The diluted PS bead solution (50 μL) was drop cast onto a plasma cleaned glass surface.

Hydrogel preparation: Poly N-isopropylacrylamide-co-allylamine (pNIPAM-co-AA) hydrogels were synthesized by free-radical polymerization following previously published methods.[49, 50] Plasma cleaned glass samples were coated with a thin layer of pNIPAM polymer by spin coating 50 μl 1% pNIPAM in water solution to reduce non-specific interaction of the proteins with the glass surface. Synthesized pNIPAM-co-AA hydrogels were roughly spherical in shape and approximately 700 nm in diameter as measured by dynamic light scattering. The hydrogels were dispersed in water and spin coated on top of the pNIPAM film for protein interaction on the hydrogel experiments. The dispersed hydrogels were vortexed before spin coating and the concentration was maintained so that they are well-separated on the pNIPAM polymer surface. The spherical shape of the hydrogels makes them ideal test samples for 3D interaction of proteins on porous polymers.

Protein preparation: Rhodamine B labeled lysozyme C (Nanocs) solutions (0.5 nM) were freshly prepared in 10mM HEPES (pH 7.3) buffer. The protein solution was drop cast on the hydrogels on the glass coverslips and the motion of the proteins were measured using the microscope setup described below.

Live cell cultures: Murine lung cells (mesenchymal 344SQ cells and epithelial 393P Vector cells) were a gift from the Kurie lab, UT MD Anderson Cancer Center. The cells were generated as stable transformations with ectopic expression of mCherry tagged Rab5+ early endosomes. We cultured the cells in RPMI-1640 media supplemented with 2.05 mM L-glutamine (HyClone), 10%

fetal bovine serum (HyClone), and 1% penicillin streptomycin (Corning) at 37.0 °C and maintained in a humidified CO_2 incubation chamber.

Wide-field single-molecule fluorescence imaging: Experimental data was collected on a home-built wide-field fluorescence microscope. Samples were excited with 560 nm light from a white light laser (SuperK FIANIUM) operating at a 78 MHz repetition rate, focused at the center of a high numerical aperture oil-immersion objective (100x magnification, NA = 1.46, Carl-Zeiss, alpha Plan-Apochromat) in epi-fluorescence excitation mode. Fluorescence signal was collected with the same objective, filtered with a dichroic mirror (Chroma, z532/633rpc), then focused with a tube lens (f = 165 mm). The optical signal was transferred into a 4f system consisting of two lenses (f = 100 mm) with a DH phase mask (Double Helix LLC) located in the center to access the Fourier plane. The phase mask convolved signal was recorded using a back-illuminated sCMOS camera (Photometrics Prime 95B, 600x600 pixel area, 68.5 nm pixel size) operating at 30 ms per frame. Polystyrene bead and lysozyme samples were imaged at 30 ms exposure for 1000 frames with 2 mW of 560 nm laser power before the objective. The incident excitation intensity at the sample was around 0.08 mW/cm^2.

Cellular imaging: Cells were seeded one day before measurement on a 35 mm glass bottom (No. 1.5) dish with a thickness of around 170 μm (MatTek Corporation). All live cell measurements were carried out with cells immersed in 1X live cell imaging solution (Invitrogen) supplemented with 0.2% bovine serum albumin (BSA), fraction V solution (GIBCO), and 5mM glucose solution (GIBCO). Cells were placed in a temperature-controlled incubation chamber (OKOLAB) maintained at 37.0 °C. A temperature-sensitive immersion oil (Immersol 518 F/370 C, ZEISS) was used to account for temperature mismatches and optical aberrations during measurements. Live

cells were imaged at 30 ms exposure for 1000 frames with 60 μW of 560 nm laser power before the objective. The incident excitation intensity at the sample was around 2.14 μW/cm^2.

Data analysis:

A high-level description of KNOT details four steps to form particle trajectories: signal to noise ratio (SNR) boosting, point cloud representation, particle identification, and trajectory linking (see Figure S1 in the Supporting Information). To begin, we equally filter the stack of raw images and a simulation of the appropriate phase mask PSF to remove amorphous backgrounds, suppress noise, and enhance the particle signal.[51, 52] The second step combines the enhanced image and phase mask to estimate particle locations as a weighted cloud of points via iterative deconvolution, using the Airy disk PSF for 2-D localization, or any of the astigmatism, double helix (DH), or tetrapod PSFs for 3-D.[21] The third step clusters the estimated point cloud into several smaller point clouds, each representing the possible locations of a detected particle. Finally, we track entire point clouds rather than representative points to capture the localization uncertainty in the single frame displacement (SFD) distributions. The linking process considers candidates within a search radius ρ_{max} from each particle to prohibit physically unlikely linkages. We rate the likelihood of each new linkage using the characteristic SFD distribution across a sliding window of previous frames, building a trajectory from the most likely linkages. The combination of maximum a posteriori estimation and a sliding window allows KNOT to avoid using a predetermined motion model to construct trajectories, capturing particles despite switches between directed and diffusive transport. Details of each step follow. Additionally, runtime data is available in Tables S1 and S2 in the Supporting Information.

Phase engineering for 3-D imaging requires deconvolution to localize: Phase engineering makes it possible to localize in 3-D from a 2-D image by manipulating the PSF, but this process

introduces new challenges (Figure 1). Capturing axial information is possible with a range of techniques such as multiple focal planes and light sheets, as recently reviewed.[21] For traditional wide-field microscopy, though, there is no axial information in the 2-D image (Figure 1A). PSF engineering is one way to encode the 3-D position of particles to capture a complete description of intracellular vesicle dynamics (Figure 1B). For example, a DH phase mask captures axial motion by modulating the PSF via the Fourier plane (Figure 1C), encoding particle depth in the azimuthal angle between two lobes.[13, 19, 20, 22-24] Single particle axial positions are recovered without incident (Figure 1D left), but PSF overlapping introduces pairing ambiguities when the dual lobes highlight overlapping particles, or multiple particles are present in proximity (Figure 1D center, right). Extremely high densities such as what is shown in Figure 1D, right, are difficult to resolve accurately regardless of the method used and may require deep neural networks[20] or other sophisticated localization methods. Naïve lobe-pairing approaches fail to localize overlapping lobes (Figure 1E left). We overcome the PSF overlapping problem by using deconvolution (Figure 1E right), which assigns a probability to all possible localizations based on matching intensity profiles to PSF templates, selecting the solution that reconstructs the image using as few particles as possible. To perform deconvolution, we iteratively maximize reconstruction accuracy and minimize the recovered particle density using the optimization problem presented in Equation 1:

$$\min_{x} \|y - \Sigma_z(x * k)\|_2^2 + \lambda_1 \|x\|_1 \quad (1)$$

where y is the observed 2-D image, x is the estimated weighted 3-D particle distribution, k is the set of 2-D PSF templates stacked as a 3-D matrix, and λ_1 is the regularization parameter set to unity (see Section 3 in the Supporting Information). In this work, k is the simulated DH PSF as described in Figure S2 in the Supporting Information. The first term of Equation 1 evaluates the

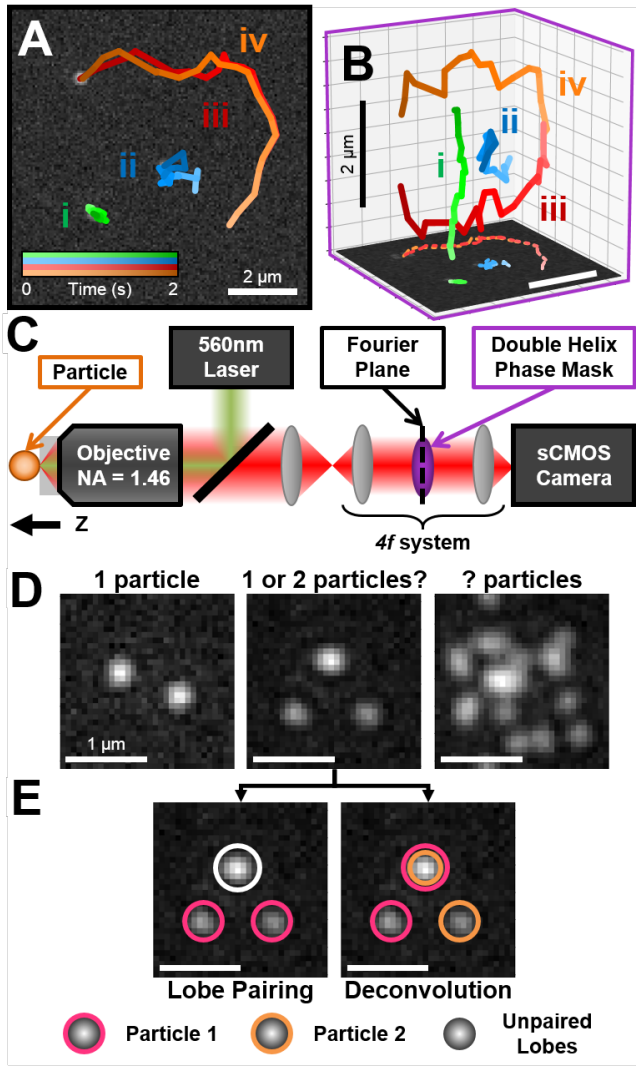

Figure 1: Phase engineering allows 3-D tracking but presents particle localization challenges. A) Simulation of particles exhibiting diffusive (i), axially directed (ii), or mixed (iii, iv) transport. B) Phase engineering encodes the true 3-D particle locations in 2-D for later reconstruction. C) A schematic of the physical widefield fluorescence setup used in DH microscopy. D) A single DH PSF is resolved by pairing lobes (left). Two or many particles experiencing overlapping PSFs present localization ambiguities (center, right). E) Localization results from identifying and pairing lobes (left) and from deconvolution (right). Abbreviations: NA, numerical aperture; sCMOS, scientific complimentary metal-oxide-semiconductor.

least squares error between the observed image and the reconstructed image, while the second term evaluates the sparsity of the estimated particle distribution. We solve this optimization problem iteratively using the Alternating Direction Method of Multipliers (ADMM)[18] (see Figure S3 in the Supporting Information). Figure S4 in the Supporting Information shows the true and KNOT localizations for each image in Figure 1D.

SNR boosting: Single molecule imaging often contains weak fluorescent signals accompanied by background and noise, requiring isolation of the in-focus signal. For accurate particle detection via deconvolution in low SNR, we apply a high-pass local background subtraction filter followed by a matched filter for noise suppression.[53] We apply the filter identically to the observed image and the phase mask kernel for optimal reconstruction of the particle distribution

(see Figure S5 in the Supporting Information).[18] Similarly, to accommodate variations in noise levels, we implement a local threshold based on the local variance around each pixel, which outperforms a global threshold for particle detection in variable SNR (see Figure S6 in the Supporting Information).

Point cloud representation: We estimate potential particle locations by considering the deconvolved particle distribution as a point cloud. We perform iterative deconvolution using ADMM, which involves a four-step process: guessing a solution, reconstructing the estimated image, comparing the reconstruction to the observed image, and scoring the reconstruction to decrease the error in our solution (Figure 2A). We illustrate this process using a single frame from the example image from Figure 1E. To begin, ADMM generates a point cloud encompassing all possible solutions for each particle position in space, assigning a small confidence to each point (Figure 2B). This point cloud initialization process results in a scattered point cloud across the solution volume, regardless of the content of the image to be deconvolved. ADMM condenses the overall point cloud with each iteration (Figure 2C) by increasing confidence in solutions that improve reconstruction accuracy and decreasing confidence in spurious solutions to enforce an overall sparse solution. As ADMM iterates, the point cloud may converge on possible particle locations, allowing for the point cloud to be segmented as described in the particle identification section below (Figure 2C inset). An example of this segmentation is shown in Figure 2D with pink and orange points corresponding to two suggested particle positions closest to the ground truth and blue points referring to other spurious solutions not seen in later iterations. In this work, we refine our estimates for 240 iterations, resulting in only two suggested particle positions after clustering (Figure 2E, also see Figure S3 in the Supporting Information).

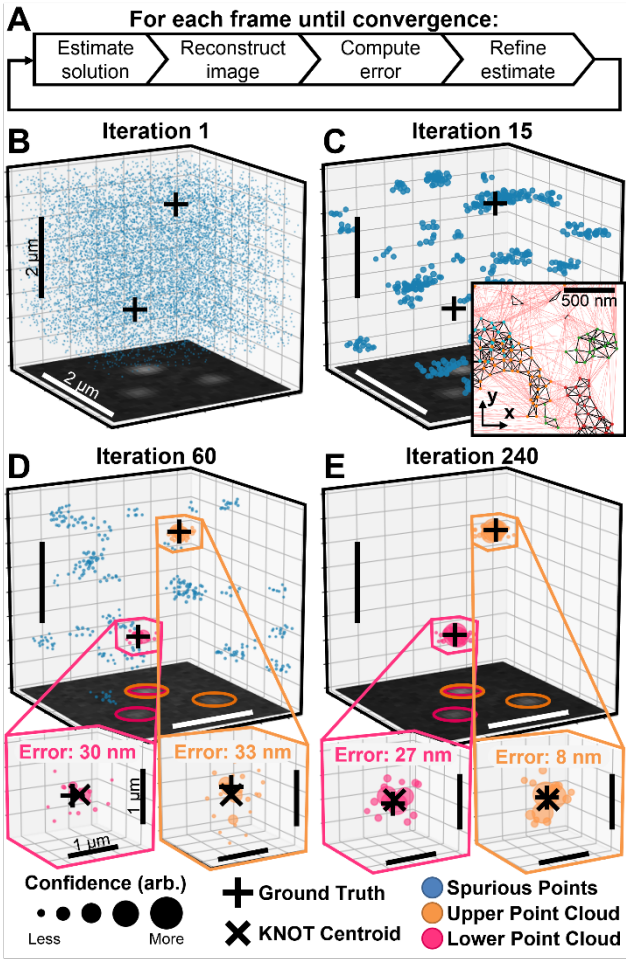

Figure 2: KNOT utilizes ADMM to reconstruct 3-D particle locations from a single frame. A) The point cloud refinement procedure. B) The solutions from the first iteration form a point cloud spanning the solution volume. C) Subsequent iterations remove spurious points from the cloud. (Inset) 2D projection of Delaunay clustering, used to segment the point cloud into sub-clouds for each particle identified. See Figure S7 in the Supporting Information. D) Refinement permits segmentation of the point cloud into clusters. (Below) The clusters nearest the ground truth positions with estimated localizations and associated errors. E) ADMM converges on a super-resolved solution for each particle position. (Below) The localization error for each cluster is smaller than previous iterations.

Particle identification: We identify particles after deconvolution in 2-D or 3-D by clustering weighted solutions into amorphous point clouds, retaining motion blur artifacts without affecting localization accuracy or precision (Figure 2). We cluster the refined point cloud (Figure 2C inset, see Figure S7 in the Supporting Information) to obtain smaller point clouds representing the 3-D particle locations for each particle (Figure 2D, 2E insets). During this process, KNOT determines the number and position of each particle for each frame analyzed independently after ADMM has iterated 240 times. When necessary, our amorphous point cloud detection scheme super-resolves particle locations by reporting the point cloud centroid (pixel size: 68.5 nm). Figure S8 in the Supporting Information illustrates the localization precision as a function of axial position, while Figure S3 shows how the localization precision changes with SNR and particle density for simulated random arrangements of particles

in 3-D. Distortions in the point clouds provide information about particle motion otherwise lost when point clouds are condensed into a single point. Retaining the point cloud and distortion enables adaptive tracking by generating a distribution of SFDs that incorporate the motion information encoded in the point cloud distortion without compromising particle identification (see Figure S7 in the Supporting Information). An example of KNOT localizing the two particles shown in Figure 2 with imperfect PSF overlap is shown in Figure S9.

Trajectory linking: We measure the displacement between point clouds to statistically define the range of possible displacements of each particle, forming SFD distributions that incorporate artifacts like motion blur into possible past localizations for the particle. Each SFD contains the motion parameters of distance (ρ), polar angle (θ), and azimuthal angle (φ) that a particle travels between two consecutive frames using spherical coordinates (Figure 3). Common tracking methods such as TrackMate[35] or MOSAIC [25] evaluate the SFD between representative localizations found by averaging point clouds[18, 25, 34, 35, 54] while others like uTrack[26] fit point clouds to a Gaussian or elliptical shape.[26, 38, 42, 51] In contrast, KNOT identifies possible candidates within a search radius ρ_{max} of the current position (Figure 3A inset) and fully connects each pair of point clouds between frames (Figure 3A) to develop distributions of ρ, φ, and θ that direct selection of the next point in a trajectory (Figure 3A, right). SFD parameter distributions are fit with a Lorentzian kernel density estimation (KDE) to form a continuous distribution of possible values, emphasizing experimental observations while permitting the possibility of large deviations through the inclusion of the Lorentzian tail.[55, 56] Particle inaction between frames is indicated in the ρ SFD distribution by nonzero KDE values despite ρ approaching zero. The motion of each particle is characterized without explicitly assigning a motion model by combining SFD distributions across frames.

The characteristic SFDs establish the likelihood of the particle displacing a certain distance at a given angle, thereby predicting where each particle will be using only a sliding window of past information. Candidates within the search radius of the current position are evaluated through a weighted maximum a posteriori estimator predicated on the characteristic SFDs of ρ, φ, and θ. This sliding window approach reinforces locally self-consistent behavior, making KNOT tolerant to photoblinking, overlapping trajectories, and sudden changes in direction. For example, in Figure 3B, we average the SFD distributions from the most recent $n = 6$ frames to form the characteristic SFD for each particle. However, the sliding window also incorporates conflicting behavior when the particle undergoes a transition between diffusive and directed motion during the window. Here, the characteristic SFD hybridizes the models of past and current motion by weighting both models according to the number of frames each model is present in the sliding window (see Figure S10 in the Supporting Information). Figure S11 in the Supporting Information demonstrates that a 6-frame window is sufficient to identify unique traits for each vesicle behavior identified by Sekh and coworkers.[31]

KNOT's characteristic SFDs classify observed motion as locally directed or not through correlation analysis with a peaked function such as the Lorentzian. Tracking the trajectories in Figure 1B using KNOT and observing archetypical behaviors in Figure S11 in the Supporting Information, we find that the angular characteristic SFDs of locally directed motion resemble a peaked function (Figure 3C). A single peak in the characteristic SFD arises from observing a similar range of angles of motion across multiple frames, showing an angular preference.[57] However, for non-directed motion, there is no angular preference,[57] hence averaging a sufficient number of frames will yield a uniform angular characteristic SFD. To determine which motion class a characteristic SFD belongs to, we fit a Lorentzian to the characteristic SFD and determine

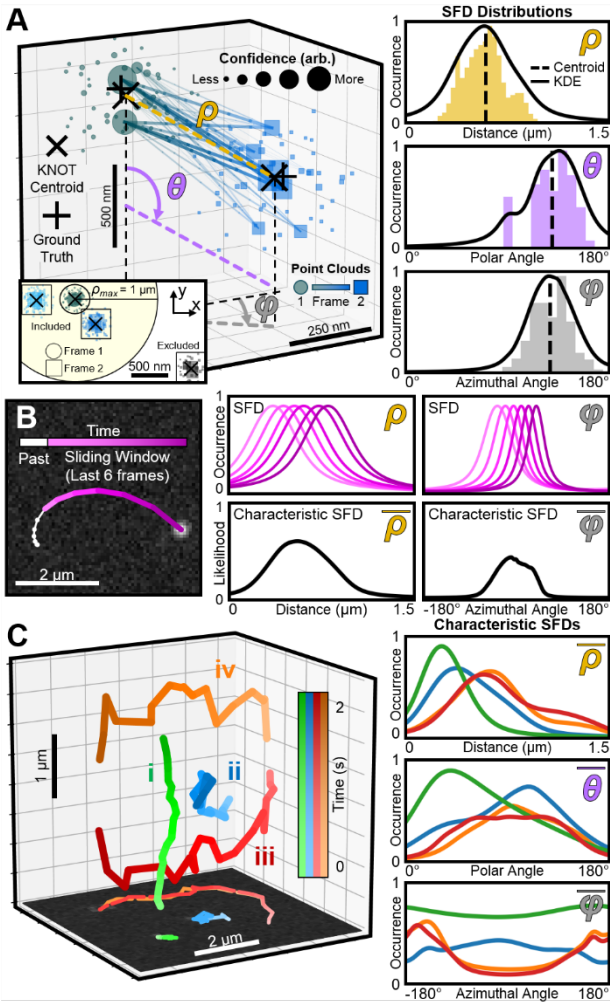

Figure 3: KNOT evaluates all SFDs between point clouds, exploiting particles affected by motion blur. A) Point clouds in two consecutive frames illustrating all possible SFDs. (Inset) Only point clouds in frame 2 within ρ_{max} of the point cloud in frame 1 are considered for SFD analysis. (Right) The SFD is parameterized into distance (ρ, yellow), polar angle (θ, purple), and azimuthal angle (φ, gray). θ and φ are defined with respect to the camera orientation. B) Simulated accelerating trajectory with marked frames inside the sliding window. (Right) The SFD distributions for each frame of the sliding window (top) are averaged to form characteristic SFD distributions (bottom). C) Simulated DH trajectories from Figure 1B for axially directed (i), diffusive (ii), and mixed motion (iii, iv) tracked by KNOT. (Right) Characteristic SFDs for each trajectory using the last 6 frames.

if the mean squared error is lower than the variance, captured by the coefficient of determination (R^2) (see section 11 of the Supporting Information). Positive values of R^2 indicate that the data is peaked, meaning the particle moved in a consistent direction during the sliding window and is likely undergoing directed transport. Conversely, negative values of R^2 mean that the directionality of particle motion was uniform in all directions, characteristic of Brownian motion. Near-zero values of R^2 require a larger sliding window to determine if the motion is locally directed or diffusive.

The spherical coordinate basis is chosen because the displacement (ρ) and orientation of motion (θ, φ) are isolated in the basis vectors, simplifying the analysis between directed motion, in which θ and φ have non-random distributions, and diffusion. Transferring to a Cartesian basis set is non-destructive and could be

performed to facilitate different analyses. In cases of 2-D anisotropic diffusion (e.g., $D_x=D_y\neq D_z$), a Cartesian basis has similar SFD distributions as for isotropic diffusion, however a spherical basis will always show angular preference. Nonetheless, if the motion is consistent and well expressed over the sliding window, we expect KNOT to accurately track particles regardless of coordinate basis.

Results and discussion:

Validation of tracking algorithm on simulated and experimental 2-D and 3-D trajectories:

We validate KNOT against three similar, high-performing methods from the 2012 IEEE International Symposium on Biomedical Imaging (ISBI) particle tracking challenge, comparing method performance across SNRs in 2-D vesicular motion[48] (see Tables S3-S10 in the Supporting Information). KNOT is shown to match or outperform methods using nearest-neighbors,[51] Kalman filtering with multiple interacting models,[42] zeroth and second moment analysis to globally minimize interparticle distance,[25, 34] and methods solving the linear assignment problem.[35] We evaluated five performance metrics representing different facets of tracking: the measure of matching tracks (α), correct/incorrect tracks (β), Jaccard similarity of points (JSC), Jaccard similarity of full tracks (JSC_θ), and the RMSE of identified points and paired tracks.[58] The Jaccard similarity coefficient is derived from the number of true positive (TP), false negative (FN), and false positive (FP) points and tracks, respectively. Tables S1-S8 in the Supporting Information illustrate the tracking performance in typical intracellular vesicle motion where diffusive behavior is prevalent with peak SNR values varying from 7 to 1. Without knowledge of expected particle motion, KNOT competes best when SNR is near or below the critical level of 4,[48, 54] challenging the best performance observed of any method given the advantage of a preordained motion model.

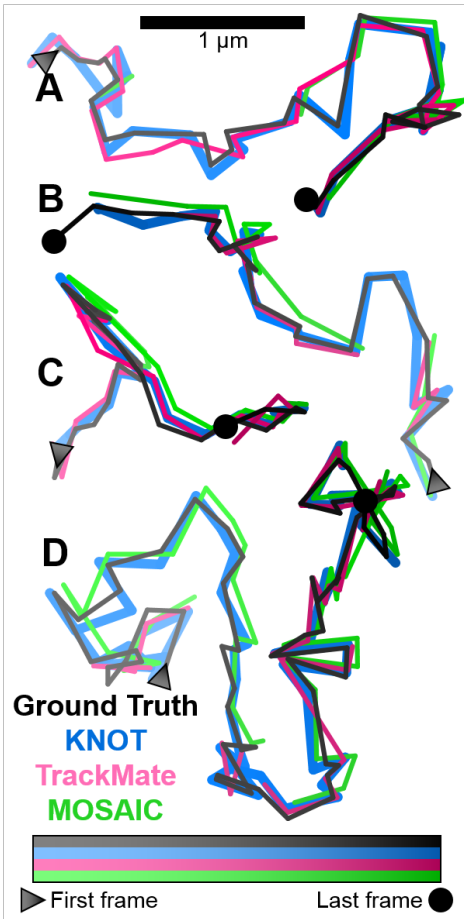

E

	Localization			Detection			
Trajectory a	α	β	RMSE	JSC	TP	FN	FP
KNOT	**0.848**	**0.848**	1.175	**1.000**	**31**	**0**	**0**
TrackMate	0.843	0.843	**0.987**	**1.000**	**31**	**0**	**0**
MOSAIC	0.214	0.201	2.827	0.457	16	15	4
Trajectory b	α	β	RMSE	JSC	TP	FN	FP
KNOT	**0.855**	**0.855**	0.990	**1.000**	**23**	**0**	**0**
TrackMate	0.474	0.403	**0.525**	0.444	12	11	4
MOSAIC	0.288	0.229	2.857	0.483	14	9	6
Trajectory c	α	β	RMSE	JSC	TP	FN	FP
KNOT	0.845	0.845	0.809	0.958	23	1	**0**
TrackMate	**0.869**	**0.869**	**0.737**	**1.000**	**24**	**0**	**0**
MOSAIC	0.411	0.411	2.414	0.680	17	7	1
Trajectory d	α	β	RMSE	JSC	TP	FN	FP
KNOT	**0.804**	**0.765**	0.911	**0.885**	**54**	**4**	**3**
TrackMate	0.225	0.161	**0.892**	0.185	15	43	23
MOSAIC	0.218	0.155	2.554	0.294	25	33	27

Adaptive Nearest Neighbors Autoregression

Figure 4. Comparison between KNOT (blue), TrackMate (pink) and MOSAIC (green) on simulated representative trajectories in SNR 2 (black). Particle motion is primarily: A) diffusive, B) directed, C) confined diffusion, D) mixed. E) The quantitative performance of each method evaluated with the ISBI 2012 metrics. Bold values indicate the best performance. RMSE in 67 nm pixels.

We also compare our adaptive tracker to two open-source ImageJ (NIH Image) tracking programs: TrackMate[35] and MOSAIC,[25] which use user-defined parameters to solve the linear assignment problem for nearest neighbors trajectory formation or track via autoregression, respectively (Figure 4). Choosing each method represents a comparison to algorithms that excel at finding diffusive and directed motion in low SNR. We select four representative trajectories from the SNR 2 vesicle dataset exhibiting diffusive (Figure 4A), directed (Figure 4B), confined diffusion (Figure 4C), and mixed motion (Figure 4D) to evaluate each method. TrackMate competes with KNOT on diffusive trajectories but prematurely severs trajectories that involve directed motion. In the directed and mixed trajectories, TrackMate outperforms KNOT in RMSE because the RMSE calculation favors conservative point

detection.[58] In contrast, MOSAIC finds simpler representations of the trajectory consistent with an autoregression model but avoids sharp changes in velocity that KNOT correctly captures. KNOT balances performance across diffusive and directed motion without the need for input bias, providing better results on samples where particles exhibit different motions or change transport during observation

We show that KNOT improves upon our previous 3-D DH tracking system, Troika-DH,[51] in one simulated and three experimental DH imaging scenarios (Figure 5). The first scenario simulates mixed motion and trajectory overlap given a high peak SNR of 9.7 and temporal resolution of 10 ms per frame. Troika-DH detects each particle present but only tracks the particle if no other particle is nearby (Figure 5A). KNOT improves performance by using the most likely positions for particles, even in cases of overlap (Figure 5B). The first experimental scenario uses polystyrene beads fixed to a pre-programmed piezoelectric stage to emulate directed trajectories with sharp turns in ideal experimental settings (peak SNR 5.0). Troika-DH captures the directed particle motion, but prematurely terminates trajectories while in motion (Figure 5C). KNOT improves tracking performance by predicting where particles will be, even
without detection, using the adaptive tracker (Figure 5D). The next experimental case shows how KNOT reduces false positive tracks in noisy protein tracking data, on movies of lysozyme adsorption on pNIPAM-co-AA polymer with a peak SNR of 3.5. Experimental conditions are adjusted such that lysozyme desorption times from pNIPAM-co-AA should be approximately 60 ms, meaning that an accurate algorithm should not identify trajectories longer than 3 frames or distances longer a pixel.[50] Troika-DH spawns several spurious trajectories surrounding each adsorption site (Figure 5E) whereas the sparsity constraint during ADMM gives KNOT a concise list of particles to track (Fig 5F). The last experimental scenario tracks $Rab5^{+}$ early endosome

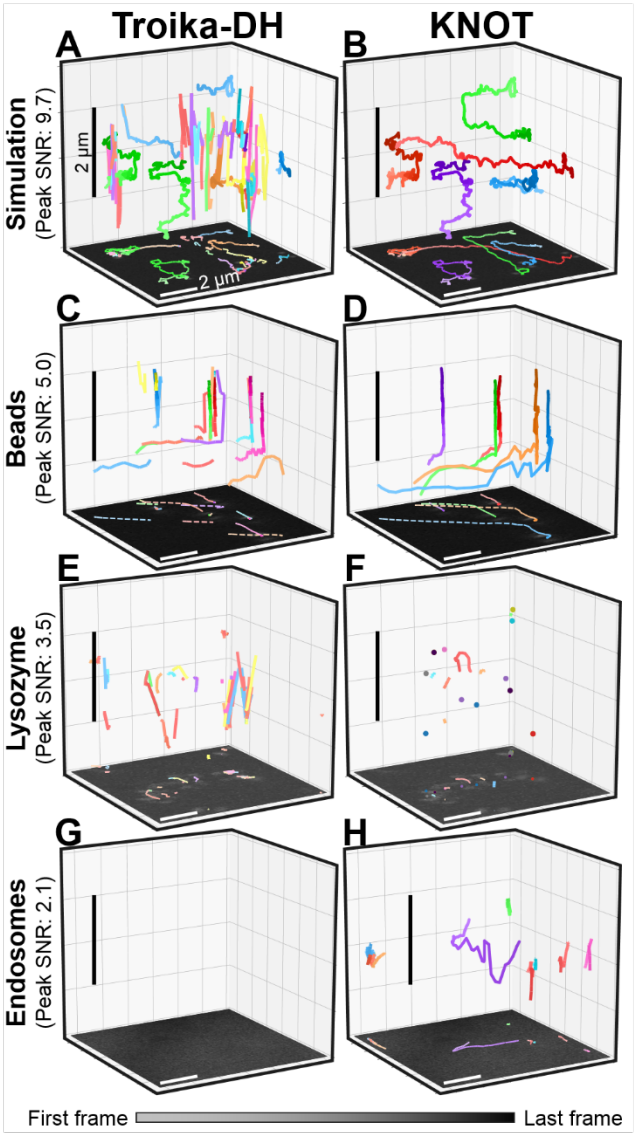

Figure 5. KNOT and Troika-DH[51] evaluated over four 3-D scenarios with differing SNR and motion types. A, B) Simulated data exhibiting particle overlap and mixed motion. C, D) Experimental data from fixed polystyrene beads on a moving piezoelectric stage. E, F) Experimental data from 1 nm lysozyme adsorbing to a pNIPAM-co-AA surface. Images have been enhanced for visualization purposes only. G, H) Experimental data from mCherry tagged Rab5^{+} early endosomes in a live cell (murine 344SQ mesenchymal cells).

dynamics in murine 344SQ mesenchymal live cells with dynamic backgrounds, variable noise levels (peak SNR of 2.1), and mixed particle motion. The low SNR forbids detection of any particle using Troika-DH (Figure 5G), but improved preprocessing allows KNOT to isolate three endosomes from the complex background exhibiting confined diffusion and mixed directed motion (Figure 5H). As shown, KNOT greatly improves upon our previous method by using local, model-less approaches to detection and tracking.

SFD analysis classifies locally diffusive and directed endosomal motion in live cells: KNOT is applied to track intracellular early endosomal dynamics, which are known to exhibit complex motions[30, 59] including switching between diffusive and directed motion (Figure 6). State-of-the-art particle motion classification methods often rely on MSD analysis to identify trajectories or trajectory segments exhibiting consistent diffusive or directed

motion over tens or hundreds of frames.[60] Conventional MSD analysis compares the average squared distance between all points in a trajectory as a function of the time difference τ to a power law: $MSD(\tau) = C\tau^{\alpha}$, where C and α are fitting parameters.[60] Figure 6A and 6B contain representative examples of diffusive and directed motion, respectively, and the associated MSD curve. MSD analysis is effective to classify trajectory motion containing a singular type through the power law exponent, with Ahmed and coworkers selecting $\alpha = 1.4$ as the boundary between directed ($\alpha > 1.4$) and diffusive ($\alpha < 1.4$) motion.[57] However, a single power law fails to capture the intricacies of mixed motion (Figure 6C), leading the development of the tMSD, which evaluates the MSD along a sliding window.[57] A sliding window accommodates mixed motion provided the duration of the window is small compared to the duration of the trajectory. KNOT exploits the information captured in point clouds to shorten the window to as few as 6 frames while distinguishing between diffusive, directed, and mixed motion through the characteristic SFD.

We present a biological application of KNOT by classifying intracellular endosomal dynamics, extracting the fraction of directed motion that travelled axially or laterally to the measurement focal plane. Figure 6D illustrates a manual motion classification analysis of $Rab5^{+}$ early endosomes in a live epithelial (393P Vector) live cell tracked using KNOT, thereby exposing the associated point clouds with each trajectory. The local motion of each particle was classified by observing the trajectory of the particle for 20 frames. The particle motion was then classified as either directed or diffusive based on if the particle moved linearly or repeatedly changed direction, respectively. To check for misclassifications, we compared our classifications to random forest analysis[61] trained on simulated mixed motion, stochastically transitioning between directed and diffusive motion, indicates around 80% agreement with our manual classification (see Figure S12 in the supporting information for more details). The disagreement appears when diffusing

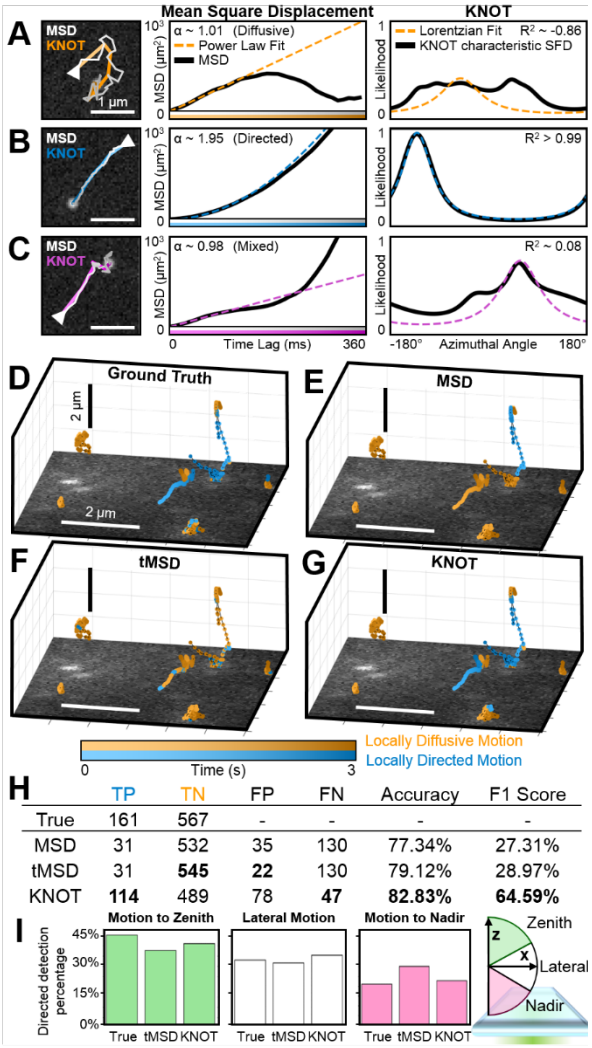

Figure 6. KNOT more accurately classifies locally diffusive and directed motion in Rab5⁺ vesicles exhibiting mixed motion than MSD or tMSD analysis. Representative trajectories, MSD analysis, and KNOT analysis for A) diffusive, B) directed, and C) mixed motion. MSD analysis uses 37 frames at 5 ms intervals while KNOT uses 7 frames at 30 ms intervals. Motion classification for 8 trajectories containing 728 detections via D) manual classification, E) MSD analysis, F) tMSD analysis, or G) KNOT analysis. H) Classification performance for each method. Directed motion is labeled as a positive result while diffusive motion is labeled as negative. I) Percentage of detections marked as part of directed motion exhibiting motion axially (left and right) or laterally (middle) measured manually, via tMSD, or KNOT. Axial motion is within 60 degrees of the z-axis.

particles briefly experienced linear motion or directed particles jittered while moving slowly, as the window only provided context for our manual classification of local motion. We analyzed the local motion of each trajectory using MSD analysis (Figure 6E), tMSD analysis (Figure 6F), and our KNOT analysis (Figure 6G). Comparing each analysis to our ground truth, we find that KNOT surpasses both methods in accuracy and F1 score (Figure 6H). Like the tMSD, KNOT classifies trajectory segments as diffusive or not rather than entire trajectories, enabling mixed motion analysis. We further classify locally directed motion as towards the zenith (i.e., away from the coverslip), lateral, or towards the nadir (i.e., towards the coverslip) with respect to the measurement focal plane, weighting each of the three angular regimes equally (Figure 6I). Comparing the true direction with the estimated directions from tMSD and KNOT

analysis, we find that endosomes preferentially transport laterally or towards the zenith (34% and 45% respectively) rather than towards the nadir (22%). As such, KNOT more accurately classifies the local motion and its direction than the preceding MSD approaches, making KNOT a valuable complement to intracellular trafficking studies especially when the number of frames is limited.

Conclusion:

This work presents KNOT, a 2-D and 3-D adaptive single particle tracking algorithm for application in obtaining and analyzing mechanistic transport of particles inside cells, at polymer interfaces, and other biologically relevant studies without bias to known models. KNOT utilizes data traditionally truncated by other tracking methods, leveraging information encoded in PSF artifacts to better classify intracellular motion and achieve higher fidelity trajectories using simpler hardware. Point clouds treat motion blur as encoded information about particle dynamics, using adaptive analysis on the SFDs produced from motion clouds to better classify the motion types. Averaging SFDs over short timescales allows KNOT to adapt to changes in particle motion, such as transitions from directed to diffusive transport in intracellular cargoes or between adsorption and diffusion in protein/polymer interactions. Requiring less frames than MSD analysis and remaining agnostic to PSF shape renders KNOT useable for cheaper, simpler instrumental configurations. Removing the need for pre-determined sample information streamlines classification of particle dynamics and paves the way for faster and more effective investigations of intracellular mechanisms. While no tracking methodology is the "best" across all experimental conditions,[48] the generalized and adaptive approach we present with KNOT is accurate and widely applicable. As a universal tracking algorithm, KNOT accommodates and explores possible model-

less behaviors by adapting to each particle individually, competing or surpassing biased state-of-the-art tracking and analysis methods.

Supporting Information:

Additional 13 sections of text, 29 equations, 12 figures, and ten tables describing (1) Computational details, (2) KNOT performs a four-step process to detect, represent, identify, and track particles, (3) Simulation of the double helix phase mask point spread function, (4) Recovery of particle locations using the Alternating Direction Method of Multipliers (ADMM), (5) Filtering the phase mask point spread function preserves the underlying particle distribution, (6) Local thresholds derived from noise statistics outperform global thresholds for particle detection, (7) Delaunay clustering identifies particles without shape expectations, (8) How localization precision changes with axial position and PSF overlap, (9) How the number of historical frames n affects KNOT predictions, (10) Single frame displacement distributions of common vesicle motions, (11) Motion classification using SFD analysis, (12) Quantitative comparison between tracking algorithms on 2-D ISBI 2012 datasets, and (13) Discrepancies between manual classification and random forest analysis.

Author Contributions

J.Z.O, L.D.C.B., and C.F.L conceived the approach. L.D.C.B. prototyped the tracking algorithm and performed preliminary data analysis. J.Z.O designed and implemented the tracking algorithm, performed the simulations, and analyzed the data with contributions from all authors. C.D. designed the microscope setup and prepared polystyrene beads and lysozyme on pNIPAM-co-AA. S.S.B. prepared 344SQ and 393P Vector live cells. C.D., W.L., and S.S.B. collected

data. J.Z.O, L.D.C.B., C.D., S.S.B., W.L. and C.F.L. wrote the manuscript with contributions from all authors.

Funding Sources

National Science Foundation (NSF) (CHE-1808382); Welch Foundation (C-1787); National Science Foundation Graduate Research Fellowship Program (1450681).

Notes

The authors declare no competing financial interest.

The code is made publicly available at https://github.com/LandesLab/KNOT.

Acknowledgements:

J.Z.O, C.D., W.L., and C.F.L. thank the National Science Foundation (grant no. CHE-1808382) and the Welch Foundation (grant no. C-1787). L.D.C.B. acknowledges the support by the National Science Foundation Graduate Research Fellowship Program (grant no. 1450681). S.S.-B. acknowledges the support from Rice University. This work was concluded in part using resources of the Shared Equipment Authority (SEA) at Rice University. The authors thank all the members of the Landes research group, Prof. Stephan Link, and his research group for helpful discussions. The authors also thank the Kurie group at UT M.D. Anderson Cancer Center for kindly providing biological cell samples.

Abbreviations:

KNOT, Knowing Nothing Outside Tracking; PSF, point spread function; pNIPAM-co-AA, poly N-isopropylacrylamide-co-allylamine; MSD, mean squared displacement; tMSD, temporal mean squared displacement; SNR, signal to noise ratio; DH, double helix; SFD, single frame displacement; ADMM, alternating direction method of multipliers; NA, numerical aperture; sCMOS, scientific complimentary metal-oxide-semiconductor; KDE, kernel density estimation; ISBI, International Symposium on Biomedical Imaging; JSC, Jaccard similarity coefficient; RMSE, root mean-squared error.

References:

1. Levitan, E. S.; Lanni, F.; Shakiryanova, D., In vivo imaging of vesicle motion and release at the Drosophila neuromuscular junction. *Nat. Protoc.* **2007,** *2* (5), 1117-1125.
2. Tokarev, A. A.; Alfonso, A.; Segev, N., Overview of intracellular compartments and trafficking pathways. In *Trafficking Inside Cells*, Springer: 2009; pp 3-14.
3. Lippincott-Schwartz, J.; Roberts, T. H.; Hirschberg, K., Secretory protein trafficking and organelle dynamics in living cells. *Annu. Rev. Cell Dev. Biol.* **2000,** *16* (1), 557-589.
4. Rosazza, C.; Buntz, A.; Rieß, T.; Wöll, D.; Zumbusch, A.; Rols, M.-P., Intracellular tracking of single-plasmid DNA particles after delivery by electroporation. *Mol. Ther.* **2013,** *21* (12), 2217-2226.
5. Lee, Y.; Phelps, C.; Huang, T.; Mostofian, B.; Wu, L.; Zhang, Y.; Tao, K.; Chang, Y. H.; Stork, P. J.; Gray, J. W.; *et al.*, High-throughput, single-particle tracking reveals nested membrane domains that dictate KRasG12D diffusion and trafficking. *eLife* **2019,** *8*.
6. Zagato, E.; Forier, K.; Martens, T.; Neyts, K.; Demeester, J.; Smedt, S. D.; Remaut, K.; Braeckmans, K., Single-particle tracking for studying nanomaterial dynamics: applications and fundamentals in drug delivery. *Nanomedicine* **2014,** *9* (6), 913-927.
7. Shen, H.; Tauzin, L. J.; Baiyasi, R.; Wang, W.; Moringo, N.; Shuang, B.; Landes, C. F., Single Particle Tracking: From Theory to Biophysical Applications. *Chem. Rev.***2017**.
8. Bishop, L. D. C.; Landes, C. F., From a Protein's Perspective: Elution at the Single-Molecule Level. *Acc Chem Res* **2018,** *51* (9), 2247-2254.
9. Wirth, M. J.; Swinton, D. J.; Ludes, M. D., Adsorption and Diffusion of Single Molecules at Chromatographic Interfaces. *J. Phys. Chem. B* **2003,** *107* (26), 6258-6268.
10. Cooper, J. T.; Peterson, E. M.; Harris, J. M., Fluorescence imaging of single-molecule retention trajectories in reversed-phase chromatographic particles. *Anal. Chem.* **2013,** *85* (19), 9363-9370.
11. Cooper, J.; Harris, J. M., Fluorescence-correlation spectroscopy study of molecular transport within reversed-phase chromatographic particles compared to planar model surfaces. *Anal. Chem.* **2014,** *86* (23), 11766-11772.

12. Li, Y.; Hu, Y.; Cang, H., Light Sheet Microscopy for Tracking Single Molecules on the Apical Surface of Living Cells. *J. Phys. Chem. B* **2013,** *117* (49), 15503-15511.
13. Gustavsson, A.-K.; Petrov, P. N.; Lee, M. Y.; Shechtman, Y.; Moerner, W. E., 3D single-molecule super-resolution microscopy with a tilted light sheet. *Nat. Comm.* **2018,** *9* (1).
14. Konopka, M. C.; Weisshaar, J. C., Heterogeneous Motion of Secretory Vesicles in the Actin Cortex of Live Cells: 3D Tracking to 5-nm Accuracy†. *J. Phys. Chem. A* **2004,** *108* (45), 9814-9826.
15. Abrahamsson, S.; Chen, J.; Hajj, B.; Stallinga, S.; Katsov, A. Y.; Wisniewski, J.; Mizuguchi, G.; Soule, P.; Mueller, F.; Darzacq, C. D.; *et al.*, Fast multicolor 3D imaging using aberration-corrected multifocus microscopy. *Nat. Methods* **2013,** *10* (1), 60-63.
16. Ram, S.; Kim, D.; Raimund; E, 3D Single Molecule Tracking with Multifocal Plane Microscopy Reveals Rapid Intercellular Transferrin Transport at Epithelial Cell Barriers. *Biophys. J.* **2012,** *103* (7), 1594-1603.
17. Juette, M. F.; Bewersdorf, J., Three-Dimensional Tracking of Single Fluorescent Particles with Submillisecond Temporal Resolution. *Nano Lett.* **2010,** *10* (11), 4657-4663.
18. Shuang, B.; Wang, W.; Shen, H.; Tauzin, L. J.; Flatebo, C.; Chen, J.; Moringo, N. A.; Bishop, L. D. C.; Kelly, K. F.; Landes, C. F., Generalized recovery algorithm for 3D super-resolution microscopy using rotating point spread functions. *Sci. Rep.* **2016,** *6*, 30826.
19. Pavani, S. R. P.; Thompson, M. A.; Biteen, J. S.; Lord, S. J.; Liu, N.; Twieg, R. J.; Piestun, R.; Moerner, W. E., Three-dimensional, single-molecule fluorescence imaging beyond the diffraction limit by using a double-helix point spread function. *Proc. Natl. Acad. Sci. U. S. A.* **2009,** *106* (9), 2995-2999.
20. Nehme, E.; Freedman, D.; Gordon, R.; Ferdman, B.; Weiss, L. E.; Alalouf, O.; Naor, T.; Orange, R.; Michaeli, T.; Shechtman, Y., DeepSTORM3D: dense 3D localization microscopy and PSF design by deep learning. *Nat. Methods* **2020**.
21. Zhong, Y.; Wang, G., Three-Dimensional Single Particle Tracking and Its Applications in Confined Environments. *Annual Review of Anal. Chem.* **2020,** *13* (1).
22. Lew, M.; Thompson, M.; Badieirostami, M.; Moerner, W. E., *In vivo three-dimensional superresolution fluorescence tracking using a double-helix point spread function*. SPIE: 2010; Vol. 7571.
23. Lew, M.; Von Diezmann, A. R. S.; Moerner, W. E., Easy-DHPSF open-source software for three-dimensional localization of single molecules with precision beyond the optical diffraction limit. *Protocol Exchange* **2013**.
24. Shechtman, Y.; Weiss, L. E.; Backer, A. S.; Lee, M. Y.; Moerner, W. E., Multicolour localization microscopy by point-spread-function engineering. *Nat. Photonics* **2016,** *10* (9), 590-594.
25. Sbalzarini, I. F.; Koumoutsakos, P., Feature point tracking and trajectory analysis for video imaging in cell biology. *J. Struct. Biol.* **2005,** *151* (2), 182-195.
26. Jaqaman, K.; Loerke, D.; Mettlen, M.; Kuwata, H.; Grinstein, S.; Schmid, S. L.; Danuser, G., Robust single-particle tracking in live-cell time-lapse sequences. *Nat. Methods* **2008,** *5* (8), 695-702.
27. Chetverikov, D.; Verestói, J., Feature Point Tracking for Incomplete Trajectories. *Computing* **1999,** *62* (4), 321-338.
28. Lysy, M.; Pillai, N. S.; Hill, D. B.; Forest, M. G.; Mellnik, J. W. R.; Vasquez, P. A.; McKinley, S. A., Model Comparison and Assessment for Single Particle Tracking in Biological Fluids. *J Am Stat Asso* **2016,** *111* (516), 1413-1426.

29. Hatta, E., Anomalous Diffusion of Fatty Acid Vesicles Driven by Adhesion Gradients. *J. Phys. Chem. B* **2008,** *112* (29), 8571-8577.
30. Ahmed, W. W.; Saif, T. A., Active transport of vesicles in neurons is modulated by mechanical tension. *Sci. Rep.* **2014,** *4*, 4481.
31. Sekh, A. A.; Opstad, I. S.; Brigisdottir, A. B.; Myrmel, T.; Ahluwalia, B. S.; Agarwal, K.; Prasad, D. K., Learning nanoscale motion patterns of vesicles in living cells. In *IEEE Conference on Computer Vision and Pattern Recognition (CVPR)*, Seattle, WA, USA, 2020; p 14014.
32. Tan, X.; Banerjee, P.; Guo, H.-F.; Ireland, S.; Pankova, D.; Ahn, Y.-h.; Nikolaidis, I. M.; Liu, X.; Zhao, Y.; Xue, Y.; *et al.*, Epithelial-to-mesenchymal transition drives a pro-metastatic Golgi compaction process through scaffolding protein PAQR11. *J. Clin. Investig.* **2017,** *127* (1), 117-131.
33. Hansen, A. S.; Woringer, M.; Grimm, J. B.; Lavis, L. D.; Tjian, R.; Darzacq, X., Robust model-based analysis of single-particle tracking experiments with Spot-On. *Elife* **2018,** *7*.
34. Crocker, J. C.; Grier, D. G., Methods of Digital Video Microscopy for Colloidal Studies. *J. Colloid Interface Sci.* **1996,** *179* (1), 298-310.
35. Tinevez, J.-Y.; Perry, N.; Schindelin, J.; Hoopes, G. M.; Reynolds, G. D.; Laplantine, E.; Bednarek, S. Y.; Shorte, S. L.; Eliceiri, K. W., TrackMate: An open and extensible platform for single-particle tracking. *Methods* **2017,** *115*, 80-90.
36. Zhong, Y.; Zhao, L.; Tyrlik, P. M.; Wang, G., Investigating Diffusing on Highly Curved Water–Oil Interface Using Three-Dimensional Single Particle Tracking. *J. Phys. Chem. C* **2017,** *121* (14), 8023-8032.
37. Shav-Tal, Y.; Darzacq, X.; Shenoy, S. M.; Fusco, D.; Janicki, S. M.; Spector, D. L.; Singer, R. H., Dynamics of Single mRNPs in Nuclei of Living Cells. *Science* **2004,** *304* (5678), 1797-1800.
38. Applegate, K. T.; Besson, S.; Matov, A.; Bagonis, M. H.; Jaqaman, K.; Danuser, G., plusTipTracker: Quantitative image analysis software for the measurement of microtubule dynamics. *J. Struct. Biol.* **2011,** *176* (2), 168-184.
39. Ritter, C.; Wollmann, T.; Lee, J.; Bartenschlager, R.; Rohr, K. In *Deep Learning Particle Detection for Probabilistic Tracking in Fluorescence Microscopy Images*, 2020 IEEE 17th International Symposium on Biomedical Imaging (ISBI), 3-7 April 2020; 2020; pp 977-980.
40. Sergé, A.; Bertaux, N.; Rigneault, H.; Marguet, D., Dynamic multiple-target tracing to probe spatiotemporal cartography of cell membranes. *Nat. Methods* **2008,** *5* (8), 687-694.
41. Chenouard, N.; Bloch, I.; Olivo-Marin, J., Multiple Hypothesis Tracking for Cluttered Biological Image Sequences. *IEEE PAMI* **2013,** *35* (11), 2736-3750.
42. Godinez, W.; Rohr, K., Tracking Multiple Particles in Fluorescence Time-Lapse Microscopy Images via Probabilistic Data Association. *IEEE Trans. Med. Imaging* **2014,** *34*.
43. Baer, T., Understand, Manage, and Prevent Algorithmic Bias, A Guide for Business Users and Data Scientists. **2019**.
44. Karslake, J. D.; Donarski, E. D.; Shelby, S. A.; Demey, L. M.; DiRita, V. J.; Veatch, S. L.; Biteen, J. S., SMAUG: Analyzing single-molecule tracks with nonparametric Bayesian statistics. *Methods* **2020**.
45. Widrow, B.; Stearns, S. D., *Adaptive Signal Processing*. Prentice-Hall: 1985.
46. Yuan, L.; Matsuyama, K.; Chiba, F.; Konno, K.; Ieee, A Study of Feature Line Extraction and Closed Frame Structure of a Stone Tool from Measured Point Cloud. *Proceedings Nicograph International 2016* **2016**, 44-51.

47. Lee, I. K., Curve reconstruction from unorganized points. *Comput. Aided Geom. Des.* **2000,** *17* (2), 161-177.
48. Chenouard, N.; Smal, I.; de Chaumont, F.; Maška, M.; Sbalzarini, I. F.; Gong, Y.; Cardinale, J.; Carthel, C.; Coraluppi, S.; Winter, M.; *et al.*, Objective comparison of particle tracking methods. *Nat. Methods* **2014,** *11* (3), 281-289.
49. Lim, S.; Song, J. E.; La, J. A.; Cho, E. C., Gold Nanospheres Assembled on Hydrogel Colloids Display a Wide Range of Thermoreversible Changes in Optical Bandwidth for Various Plasmonic-Based Color Switches. *Chem. Mater.* **2014,** *26* (10), 3272-3279.
50. Dutta, C.; Bishop, L. D. C.; Zepeda O, J.; Chatterjee, S.; Flatebo, C.; Landes, C. F., Imaging Switchable Protein Interactions with an Active Porous Polymer Support. *J. Phys. Chem. B* **2020,** *124* (22), 4412-4420.
51. Shuang, B.; Chen, J.; Kisley, L.; Landes, C. F., Troika of single particle tracking programing: SNR enhancement, particle identification, and mapping. *Phys Chem Chem Phys* **2014,** *16* (2), 624-34.
52. Shuang, B.; Byers, C. P.; Kisley, L.; Wang, L.-Y.; Zhao, J.; Morimura, H.; Link, S.; Landes, C. F., Improved Analysis for Determining Diffusion Coefficients from Short, Single-Molecule Trajectories with Photoblinking. *Langmuir* **2013,** *29* (1), 228-234.
53. Turin, G., An introduction to matched filters. *IEEE Trans. Inf. Theory* **1960,** *6* (3), 311-329.
54. Cheezum, M. K.; Walker, W. F.; Guilford, W. H., Quantitative Comparison of Algorithms for Tracking Single Fluorescent Particles. *Biophys. J.* **2001,** *81* (4), 2378-2388.
55. Bychuk, O. V.; O'Shaughnessy, B., Anomalous Diffusion at Liquid Surfaces. *PRL* **1995,** *74* (10), 1795-1798.
56. Wang, D.; Wu, H.; Schwartz, D. K., Three-Dimensional Tracking of Interfacial Hopping Diffusion. *PRL* **2017,** *119* (26), 268001.
57. Ahmed, W. W.; Williams, B. J.; Silver, A. M.; Saif, T. A., Measuring nonequilibrium vesicle dynamics in neurons under tension. *Lab on a Chip* **2013,** *13* (4), 570-578.
58. De Chaumont, F.; Dallongeville, S.; Chenouard, N.; Hervé, N.; Pop, S.; Provoost, T.; Meas-Yedid, V.; Pankajakshan, P.; Lecomte, T.; Le Montagner, Y.; Lagache, T.; Dufour, A.; Olivo-Marin, J.-C., Icy: an open bioimage informatics platform for extended reproducible research. *Nat. Methods* **2012,** *9* (7), 690-696.
59. Scott, C. C.; Vacca, F.; Gruenberg, J., Endosome maturation, transport and functions. *Semin. Cell Dev. Biol.* **2014,** *31*, 2-10.
60. Michalet, X., Mean square displacement analysis of single-particle trajectories with localization error: Brownian motion in an isotropic medium. *Phys Rev E Stat Nonlin Soft Matter Phys* **2010,** *82* (4 Pt 1), 041914-041914.
61. Wagner, T.; Kroll, A.; Haramagatti, C. R.; Lipinski, H.-G.; Wiemann, M., Classification and Segmentation of Nanoparticle Diffusion Trajectories in Cellular Micro Environments. *PLOS ONE* **2017,** *12* (1), e0170165.

TOC Graphic:

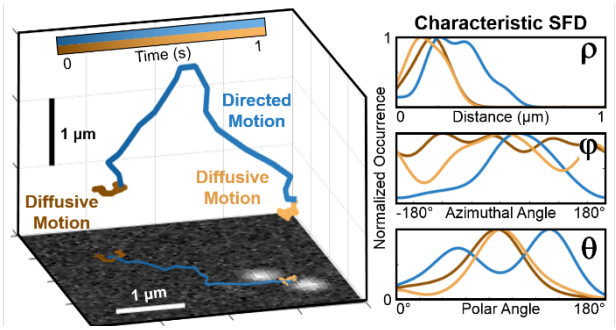
Time (s)
0
1
1 μm
Directed Motion
Diffusive Motion
Diffusive Motion
1 μm
Characteristic SFD
Normalized Occurrence
1
0
ρ
Distance (μm)
0
1
φ
-180°
Azimuthal Angle
180°
θ
0°
Polar Angle
180°